Shear wave bandgap in buckled soft laminates with stiffening phases

Mechanics of Soft Materials (2025) 7:4
https://doi.org/10.1007/s42558-025-00069-4

ORIGINAL PAPER

Shear wave bandgap in buckled soft laminates with stiffening phases

Qi Yao[1] · Stephan Rudykh[1,2]

Received: 13 April 2025 / Accepted: 10 November 2025

Abstract
This study investigates elastic instability-activated bandgaps for shear waves in soft laminates comprised of phases that exhibit stiffening. In particular, the Gent material model is used for phases. The stiff layer buckling, influenced by the stiffening behavior, results in a regulated wavy pattern along the layer direction. We analyzed how this phenomenon affects the shear wave propagation propagating along the buckled layers. Our findings exhibit that this reversible shift from an infinitely extended to a periodic structure modifies the dispersion relations and triggers shear wave bandgaps. We show that the frequency of the bandgap is closely related to the buckling state, including the wavelength and deformation level. Additionally, we explore how the bandgap can be fine-tuned by altering the material properties and geometric design of the soft laminates.

Keywords Bandgap · Elastic instability · Shear waves · Dispersion relations · Soft laminate · Metamaterial

1 Introduction

Mechanical metamaterials are a class of engineered media with dedicated micro-architectures that allow attractive functionalities induced by their structural design rather than composition. Over years of exploration, these functionalities have expanded to include auxetic behavior [1–3], reconfigurability [3–5], deployability [6], and negative thermal expansion [7]. In particular, metamaterials enlarge our abilities to tailor the properties of elastic/acoustic waves [8]. They have shown potential in various areas, such as amplifying signals [9], activating wave bandgaps [10], creating acoustic cloaks [11], and inducing negative phase [12–14] and group velocities [12, 13].

Elastic instability, commonly referred to as buckling, occurs at certain deformation levels and can be a mechanism for inducing or tuning the functionalities of metamaterials via recoverable microstructure transformation [15–18], even though it is traditionally considered a failure mode of composites [19–24]. Soft composites, which can experience large deformations, have exhibited unforeseen elastic instability-induced functionalities. Examples include honeycomb structures [25, 26], particle-reinforced composites [21, 27], and dielectric composites [28–31]. Furthermore, the interaction between elastic instability and wave propagation has opened new possibilities for acoustic functionalities in a wide variety of soft composites, such as laminates [32–34], fiber-reinforced composites (FCs) [35, 36], and substrates [37, 38].

This paper investigates activating and fine-tuning the shear wave (S-wave) bandgap via elastic instability in soft laminates with incompressible Gent phases. By incorporating predictions of instability behavior, we develop a post-buckling model and perform wave propagation analysis using the Bloch-Floquet method. A self-developed algorithm is employed to identify the S-wave bandgaps within dispersion curves. We implemented a survey to showcase the influence of geometry and material properties on the tunability of bandgaps.

The structure of this paper is as follows: Sect. 2 presents the theoretical background on wave propagation in elastic media; Sect. 3 defines the problem, introduces the 2D model of laminate under in-plane compression, and outlines the simulation framework for wave propagation analysis in post-buckled domain exhibited; Sect. 4 initially examines the underlying

✉ Qi Yao
qyao34@wisc.edu

[1] Department of Mechanical Engineering, University of WI, Madison, Madison, WI 53706, USA

[2] School of Mathematical and Statistical Sciences, University of Galway, University Road, Galway, Ireland

Published online: 22 November 2025

mechanism behind the emergence of the post-buckling bandgap for S-wave, and then investigates their dependence on material parameters; Sect. 5 summarizes our finding, highlighting key trends and observations.

2 Theoretical background

The initial position vector of material points in the solid is denoted as vector $\mathbf{X}$ in undeformed/stress-free configuration $\mathbf{\Omega}_0$. The position vector of material points in deformed configuration $\mathbf{\Omega}$ is $\mathbf{x} = \boldsymbol{\chi}(\mathbf{X})$ with $\boldsymbol{\chi}$ representing a mapping from undeformed to deformed configuration. Then, the deformation gradient tensor is $\mathbf{F} = \text{Grad}\boldsymbol{\chi}$ and $\mathbf{u}(\mathbf{x}) = \mathbf{x} - \mathbf{X}$ is the displacement of a material point. Considering hyperelastic materials with strain energy–density function (SEDF) $W(\mathbf{F})$, the first Piola–Kirchhoff (nominal) stress $\mathbf{P}$ is

$$\mathbf{P} = \frac{\partial W(\mathbf{F})}{\partial \mathbf{F}} \tag{1}$$

For incompressible materials, Eq. (1) modifies as

$$\mathbf{P} = \frac{\partial W(\mathbf{F})}{\partial \mathbf{F}} - p\mathbf{F}^{-T} \tag{2}$$

where p is the Lagrange multiplier. Correspondingly, the Cauchy stress tensor is $\boldsymbol{\sigma} = J^{-1}\mathbf{P}\mathbf{F}^T$.

With body forces absent, the equilibrium condition in the undeformed configuration is

$$\text{Div}\mathbf{P} = 0 \tag{3}$$

Following [39], the incremental deformation gradient $\dot{\mathbf{F}}$ is defined as $\dot{\mathbf{F}} = \text{Grad}\dot{\mathbf{u}}$, where $\dot{\mathbf{u}}$ is the infinitesimal incremental displacement. The incremental change in the first Piola–Kirchhoff stress $\dot{\mathbf{P}}$ can be expressed through a linearized constitutive relation

$$\dot{\mathbf{P}} = \mathbb{C}\dot{\mathbf{F}} \tag{4}$$

where $\mathbb{C}$ is the tensor of elastic moduli

$$\mathbb{C} = \frac{\partial^2 W}{\partial \mathbf{F}\partial \mathbf{F}} \tag{5}$$

Components of elastic modulus $\mathbb{C}^0$ in $\mathbf{\Omega}$ are calculated from a push-forward operation

$$C^0_{iqkp} = J^{-1}F_{pl}F_{qj}C_{ijkl} \tag{6}$$

The incremental equation of displacement is

$$\text{Div}\dot{\mathbf{P}} = \rho_0 \frac{D^2\dot{\mathbf{u}}}{Dt^2} \tag{7}$$

where $D^2()/Dt^2$ represents the material time derivative.

For the wave propagation problem, the wave frequency and wave mode can be solved by substituting the small amplitude displacement $\dot{\mathbf{u}}$ in particular form into Eq. (7).

3 Numerical analysis

We consider an incompressible laminate composed of two distinct phases, as shown in Fig. 1. Figure 1 (a) presents a 3D schematic of the laminate under in-plane compression. A corresponding 2D model, shown in Fig. 1(b), depicts the periodic distribution of stiff layers within a soft matrix along the $\mathbf{e}_1$ direction. This figure also exhibits the propagation of waves in buckled laminate.

In Fig. 1, the soft matrix and stiff layer are represented by $r = m$ and $r = f$, respectively. The volume fraction of phase r is a constant value $c^{(r)}$ due to incompressibility. A hidden relation volume fraction of both phases is $c^{(m)} = 1 - c^{(f)}$. L_0 is the

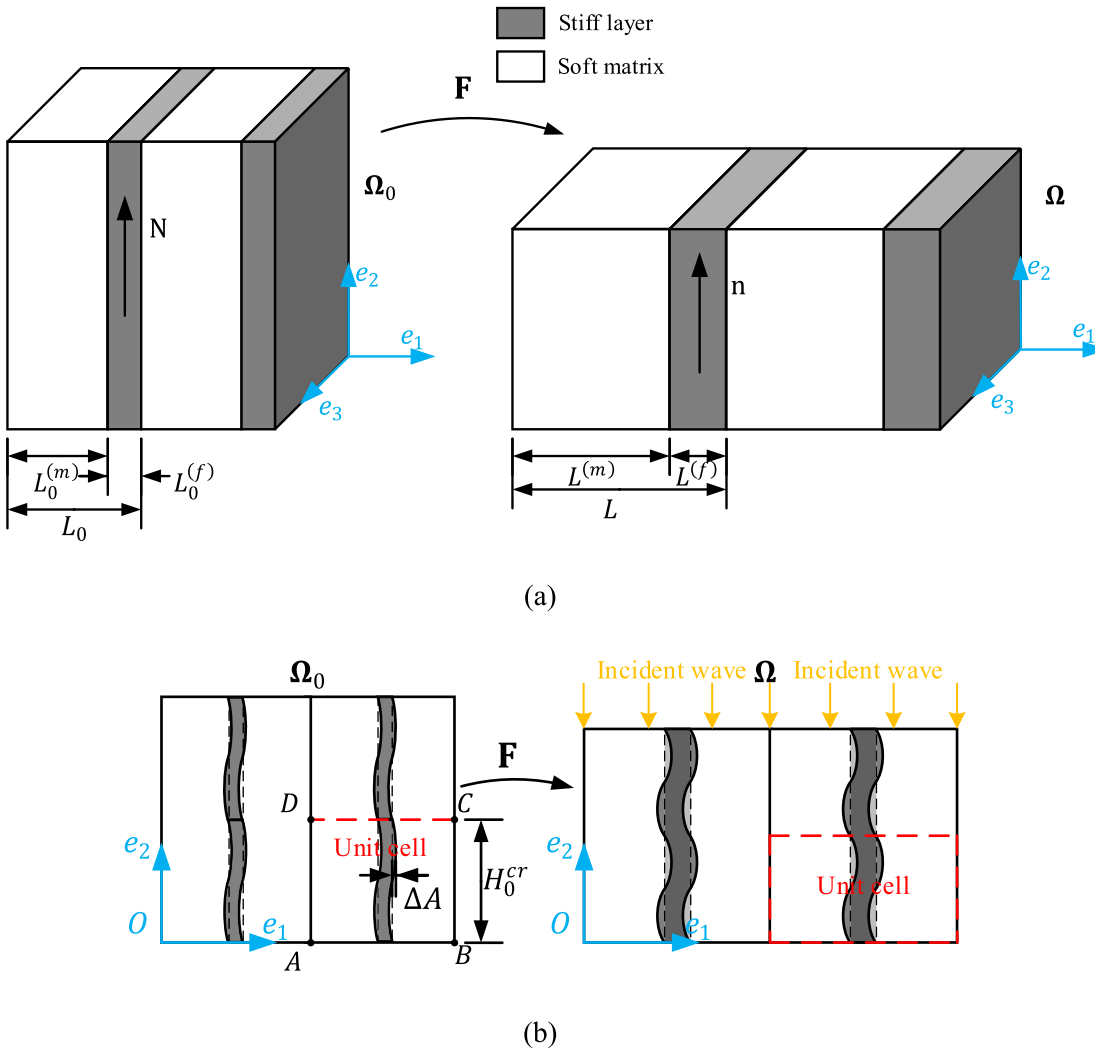

Fig. 1 **a** Schematic of 3D laminate under uniaxial compression along $\mathbf{e}_2$. **b** 2D schematic of laminate with imperfections under uniaxial compression

initial length of a unit cell in the undeformed configuration $\mathbf{\Omega}_0$ as highlighted in Fig. 1, while L is the length of a unit cell in the deformed configuration $\mathbf{\Omega}$. As a microscopic size, the characteristic size of the unit cell L_0 is assumed to be sufficiently smaller than the overall size of the laminate. Unit vectors $\mathbf{N}$ and $\mathbf{n}$ represent the direction of the stiff layer in undeformed and deformed configurations, respectively. The vector $\mathbf{N}$ is set to be the same as the Cartesian basis vector $\boldsymbol{e}_2$. Phases are homogenous hyperelastic materials characterized by the Gent strain energy density function (SEDF)

$$W^{(r)}\left(\mathbf{F}^{(r)}\right) = -\frac{\mu^{(r)} J_m^{(r)}}{2} \log\left(1 - \frac{I_1^{(r)} - 3}{J_m^{(r)}}\right) + \frac{1}{2}\kappa^{(r)}\left(J^{(r)} - 1\right)^2 \tag{8}$$

where $\mu^{(r)}$ and $\kappa^{(r)}$ are shear modulus and bulk modulus of the phase r, respectively; $J_m^{(r)}$ is the locking parameter that characterizes the material stiffening of phase r due to the limit of extensibility in the modular chain framework; $\mathbf{F}^{(r)}$ is the deformation gradient tensor and $J^{(r)} \equiv \det\mathbf{F}^{(r)}$ is the ratio between the volume of a unit cell in the deformed configuration and that in the undeformed configuration; $I_1^{(r)} \equiv \mathrm{tr}\left(\mathbf{F}^{(r)^T}\mathbf{F}^{(r)}\right) = \mathbf{F}^{(r)} : \mathbf{F}^{(r)}$ is the first invariant of the right Cauchy-Green deformation tensor $\mathbf{C}^{(r)} = \mathbf{F}^{(r)^T}\mathbf{F}^{(r)}$. The initial shear modulus contrast is defined as $k_\mu = \mu^{(f)}/\mu^{(m)}$. In the Gent model, the development of deformation leads to $\frac{I_1^{(r)}-3}{J_m^{(r)}} \to 1$ and $W^{(r)} \to +\infty$, which can be shown by the significant increase in stress components. When $J_m^{(r)}$ is set to be extremely high ($J_m^{(r)} = 10^3$, for example), Eq. (8) reduces to the neo-Hookean model

$$W^{(r)}\left(\mathbf{F}^{(r)}\right)=\frac{\mu^{(r)}}{2}\left(I_1^{(r)}-3\right)+\frac{1}{2}\kappa^{(r)}\left(J^{(r)}-1\right)^2 \tag{9}$$

To ensure the high incompressibility of phases, a bulk-to-shear ratio $\kappa^{(r)}/\mu^{(r)}=10^3$ is chosen.

The laminate is subjected to in-plane compression with homogeneous deformation gradient tensor

$$\overline{F}=\lambda^{-1}e_i,\otimes e_1+\lambda e_2+e_2+e_3\otimes e_3 \tag{10}$$

where $\boldsymbol{e}_i, i=1,2,3$ are coordinate vectors as shown in Fig. 1; λ is the macroscopic stretch along the stiff layer direction $\boldsymbol{e}_2$. The locking condition $I_1^{(r)}-3=J_m^{(r)}$ together with the deformation gradient tensor solves the locking stretch for compressed Gent phases in the following form

$$\lambda_{lock}=\max\left\{\left(\left(J_m^{(r)}+2-\left(J_m^{(r)2}+4J_m^{(r)}\right)^{1/2}\right)/2\right)^{1/2}, r=m,f\right\} \tag{11}$$

Small amplitude displacement is superimposed onto the finitely deformed domain to study the propagation of waves, as represented by Eq. (7). Due to the periodicity of laminate as shown by Fig. 1, the small amplitude displacement for solving the incremental equation of motion (Eq. (7)) is superimposed in form of Bloch waves

$$\dot{\mathbf{u}}(\mathbf{X},t)=\mathbf{U}(\mathbf{X})\exp[i(\mathbf{K}\bullet\mathbf{X}-\omega t)] \tag{12}$$

where ω is the angular frequency of the wave, $\mathbf{K}=K_1\boldsymbol{e}_1+K_2\boldsymbol{e}_2$ is the Bloch wave vector in undeformed configuration and $\mathbf{U}(\mathbf{X})$ is a periodic function that satisfies the periodicity condition

$$\mathbf{U}(\mathbf{X}+\mathbf{R})=\mathbf{U}(\mathbf{X})e^{i\mathbf{K}\bullet\mathbf{R}} \tag{13}$$

where $\mathbf{R}=R_1L\boldsymbol{e}_1+R_2H\boldsymbol{e}_2$ is an arbitrary vector with integer coordinates R_1, R_2, denoting the spatial periodicity in the undeformed configuration. L and H are the length and height of a unit cell, respectively. Studying wave propagation along $\boldsymbol{e}_2$, the Bloch wave vector $\mathbf{K}$ is simplified into $\mathbf{K}=K_2\boldsymbol{e}_2$. The Bloch wave vector $\mathbf{k}$ in the deformed configuration is calculated by $\mathbf{k}=\mathbf{F}^{-T}\mathbf{K}$. The normalized wavenumber along $\boldsymbol{e}_2$ is $\overline{K}_2$ with $\overline{K}_2=K_2H_0/(2\pi)$ in the undeformed configuration.

A model for post-buckling analysis is constructed, as shown in Fig. 1. The initial width of the stiff layer is $L_0^{(f)}=c_0^{(f)}L_0$. L_0 is set to be constantly 1 during simulation. H_0 is the initial height of the unit cell. It is set to be the same as the critical wavelength determined by instability analysis: $H_0=H_0^{cr}=L_0/\overline{K}_2^{cr}$ according to the periodicity condition. Referring to Fig. 1, the unit cell in the post-buckling state is a section that contains only one period of stiff layer wave. Moreover, the imperfection in the model is required to trigger buckling behavior. Thus, two surfaces of the stiff layer are designed to be sine functions. ΔA is the imperfection magnitude (sine function magnitude) of the stiff layer. To ensure the transition from the stable state to the buckled one onset normally, ΔA is chosen to be 10^{-5} level.

To compute the dispersion curves in the post-buckling state, a two-step Bloch-Floquet analysis is performed in COMSOL 5.5. The boundary conditions for both steps are

$$\begin{aligned}\text{Step1.}&\begin{cases}u_{1,BC}=u_{1,AD}+u_c\\ u_{2,BC}=u_{2,AD}\end{cases},\begin{cases}u_{1,DC}=u_{1,AB}\\ u_{2,DC}=u_{2,AB}-\varepsilon H\end{cases},\begin{cases}u_{1,A}=0\\ u_{2,A}=0\end{cases}\\ \text{Step2.}&\begin{cases}u_{1,AD}=u_{1,BC}\\ u_{2,AD}=u_{2,BC}\end{cases},\begin{cases}u_{1,DC}=u_{1,AB}e^{2\pi i\overline{K}_2/H_0}\\ u_{2,DC}=u_{2,AB}e^{2\pi i\overline{K}_2/H_0}\end{cases}\end{aligned} \tag{14}$$

where ε is the deformation strain. Firstly, a time-dependent quasi-static deformation for the finitely deformed unit cell is solved. Secondly, the Bloch-Floquet conditions are imposed on the post-buckling state of soft laminate and multiple orders of eigenvalues with wavenumber $\overline{K}_2$ varying from 0 to 1 are solved to form dispersion curves $\omega=\omega\left(\overline{K}_2\right)$. Here and thereafter, the densities of both phases are chosen to be identical $\rho^{(m)}=\rho^{(f)}$. The frequency ω is then normalized as $\overline{f}=\frac{\omega H_0}{2\pi}\sqrt{\rho^{(m)}/\overline{\mu}}$, where $\overline{\mu}=c^{(f)}\mu^{(f)}+c^{(m)}\mu^{(m)}$. The normalized dispersion curves $\overline{f}\left(\overline{K}_2\right)$ are applied in analyzing bandgaps. As revealed by previous works, soft composites may lose stability on macroscopic or microscopic levels. For macroscopic instability where the wavelength is significantly larger than the characteristic sizes of microstructure, the critical wavenumber $\overline{K}_2^{cr}$ is close to 0. The microscopic instability develops at length close to the size of the characteristic unit cell with critical wavenumber $\overline{K}_2^{cr}$ significantly larger than 0. Thus, micro-instability leads to the transformation of microstructure. Due to

this property, we focus on studying the influence of microstructure transformation on the post-buckling bandgap. Moreover, since we focus on S-waves, the waves are decoupled as shown in Appendix A Eq. 16.

4 Results

4.1 Mechanism of the post-buckling bandgaps in laminates

To show the mechanism underlying the activation of bandgap in buckled laminate, we exhibit the dispersion curves corresponding to the development of deformation in an all-neo-Hookean laminate, as shown in Fig. 2. The initial shear modulus contrast is $k_\mu = 100$ and the volume fraction of the stiff layer is set at $c^{(f)} = 0.06$. The normalized frequency $\bar{f}$ is plotted as a function of the normalized wave number $\overline{K}_2$ on the x-axis.

In Fig. 2, the undeformed laminate only exhibits periodicity along $\boldsymbol{e}_1$ direction. The dispersion curves display positive slopes versus normalized critical wavenumber, which indicates the positive group velocity. As the compression progresses and the macroscopic deformation stretch ratio λ approaches the critical value λ^{cr}, the eigenvalues gradually shift toward zero. Especially, some branches of the dispersion curves start to bend as the stretch ratio enters the vicinity of the critical value, eventually turning their slopes negative. While some branches bend toward the $\overline{K}_2$ axis, some others move in the opposite direction. The different bending directions cooperatively result in the formation of the bandgap when the compression surpasses the critical stretch ratio. In Fig. 2, the variation of the dispersion curves appears with the evolution of corresponding wave modes.

In the physical domain shown by Fig. 2, the onset of instability triggers the microstructural transformation in the laminate, resulting in the formation of a waved stiff layer along $\boldsymbol{e}_2$. Simultaneously, the stress field evolves into a periodic distribution. This newly established periodicity blocks the propagation of waves within a specific frequency range, thereby inducing an S-wave bandgap. The emergence of this bandgap confirms that instability-triggered microstructural transformations in soft laminates offer a novel mechanism for elastic wave filtering.

We then study the development of the S-wave bandgap versus deformation in the post-buckling state. Figure 3 (a) and (b) illustrate the variation of bandgap bounds and the dispersion curves in all-neo-Hookean laminate with $c^{(f)} = 0.06$ and $k_\mu = 100$. Here and thereafter, the lower bound is marked by dashed red curves, the upper bound is represented by solid red curves, and the bandgap is shaded in gray unless otherwise specified.

As shown in Fig. 3, increasing compressive strain beyond the critical strain ε^{cr} leads to an expanding bandgap. The dispersion diagrams in Fig. 3 (b) show that greater deformation progressively shifts the curves defining the upper bound of the bandgap upward, thereby widening the bandgap. This behavior corresponds to an increase in the amplitude of the buckled stiff layer in the physical domain, highlighting the strong dependence of the bandgap on the level of post-buckling deformation. Here and thereafter, the post-buckling deformation level $\Delta\varepsilon = \lambda^{cr} - \lambda$, where λ represents the macroscopic compression stretch, is fixed when studying the influence of material parameters on the bandgap. Noting that the bandwidth is majorly determined

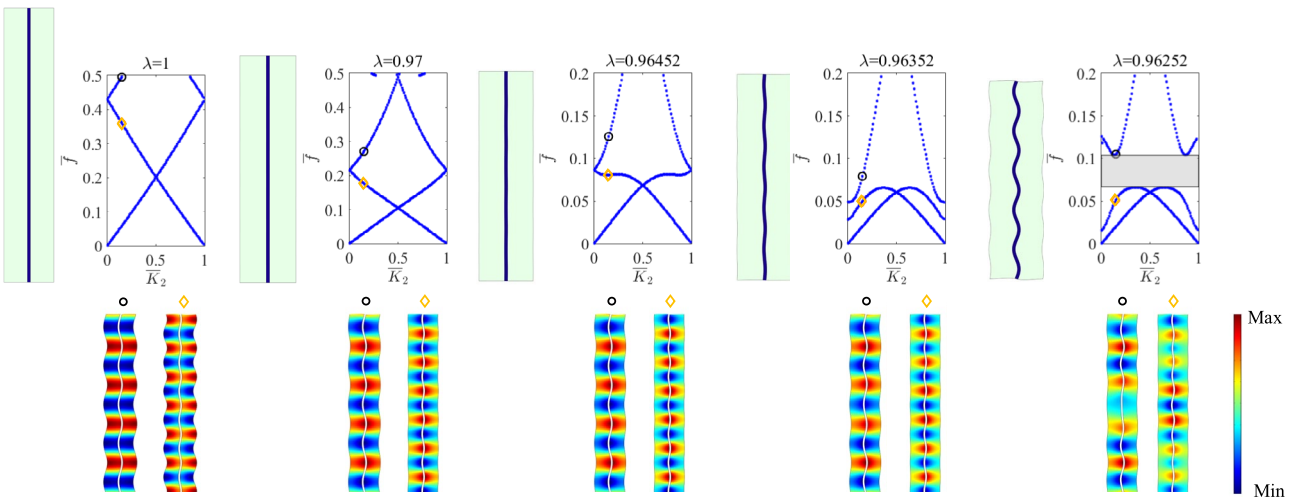

Fig. 2 Dispersion curves and deformation state versus macroscopic stretch in all-neo-Hookean laminate with k_μ = 100 and c^((f)) = 0.06; deformation scaled for straightforward observation; S-wave modes for two eigenvalues highlighted on dispersion curves are listed

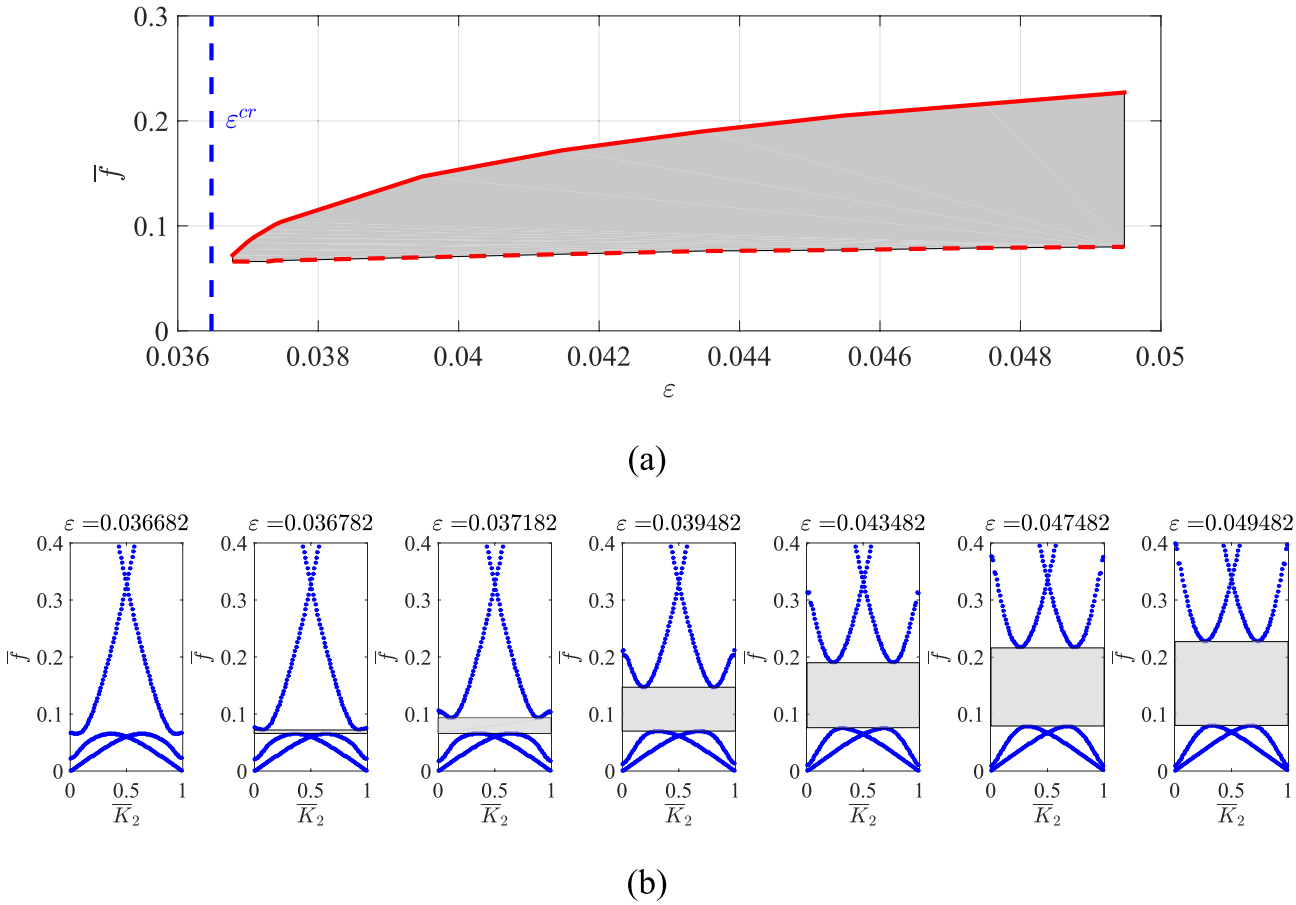

Fig. 3 **a** Bandgaps highlighted by gray region versus macroscopic stretch with lower bound marked by dashed red curves and upper bound marked by solid red curves and **b** dispersion curves in all-neo-Hookean laminates with $c^{(f)} = 0.06$, $k_\mu = 100$, and $\lambda^{cr} = 0.96352$. $\varepsilon^{cr} = 1 - \lambda^{cr}$ and normalized critical wavenumber $\bar{K}_2^{cr} = 0.89$

by deformation at high $\Delta\varepsilon$, we consider the post-buckling in the vicinity of the buckling point. It is worth concluding that the bandgap only appears after the stiff layer buckles. Thus, all subsequent analyses are only applied in post-buckling states.

4.2 Shear wave Bandgaps in laminates with Gent stiff layers

From the mechanism for activating bandgaps in post-buckled laminates, it can be forecasted that multiple factors, including the initial shear modulus contrast and locking parameters of phases , can significantly shape the bandgap. This section focuses on the bandgaps in laminates with a single phase characterized by the Gent model. In contrast to the all-neo-Hookean laminates with constant initial shear modulus contrast, those containing Gent phases (8) exhibit a deformation-dependent effective shear modulus contrast [40], adding further complexity to the relationship between modulus contrast and bandgap characteristics. We define the effective shear modulus contrast of stiff layer and matrix as

$$\hat{k}_\mu = \frac{g^{(f)}}{g^{(m)}} k_\mu \tag{15}$$

where $g^{(r)} = J_m^{(r)} / \left(J_m^{(r)} - \left(I_1^{(r)} - 3 \right) \right)$ is the stiffening parameter of phases r.

Figure 4 (a) shows a decrease in bandgap width with descending initial shear modulus contrast. A notable difference in the laminate with a Gent matrix and a neo-Hookean stiff layer is that a lower matrix locking parameter $J_m^{(m)}$ increases the disappearance threshold of the bandgap. For example, the bandgap in laminates with $J_m^{(m)} = 0.1$ disappears at approximately $k_\mu \approx 61$, which is larger than the disappearance thresholds for laminates with $J_m^{(m)} = 0.2$ and $J_m^{(m)} = 1$. In Fig. 4 (a), the bandgaps in laminate with $J_m^{(m)} = 0.2$ and $J_m^{(m)} = 1$ disappear at around $k_\mu \approx 50$, similar to the all-neo-Hookean counterparts.

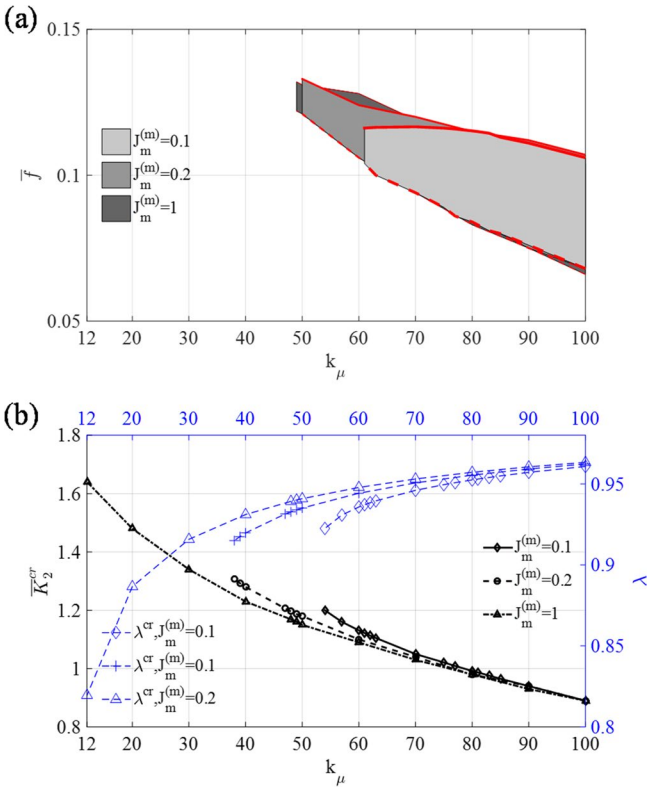

Fig. 4 **a** Bandgaps versus initial shear modulus contrast in Gent matrix and neo-Hookean stiff layer laminates with $c^{(f)} = 0.06$ and $J_m^{(m)} = 0.1, 0.2, 1$ at $\triangle\epsilon = 0.001$; **b** critical stretch and normalized critical wavenumber versus initial shear modulus contrast for laminates in **a**

When the matrix stiffens, the effective shear modulus contrast reduces. At relatively high initial shear modulus contrast ($k_\mu \approx 90 - 100$), laminates with the three different matrix locking parameters lose stability at similar critical stretches (as indicated by the closely aligned blue curves between $k_\mu = 90$ and $k_\mu = 100$ in Fig. 4 (b)). In this range, laminates buckle before the matrix stiffening significantly reduces the effective shear modulus contrast, resulting in similar bandgap widths. However, as the initial shear modulus contrast approaches the disappearance threshold of the bandgap, the increased deformation level and descending effective shear modulus contrast result in smaller bandgap widths in laminates with $J_m^{(m)} = 0.1$. On the contrary, laminates with $J_m^{(m)} = 0.2$ and $J_m^{(m)} = 1$ exhibit comparable bandgap widths until it disappears.

As exhibited by the instability analysis in Fig. 4 (b), the critical wavenumber increases with descending initial shear modulus contrast and matrix locking parameter. The decrease in initial shear modulus contrast and matrix locking parameter reduces the wavelength, thereby shifting bandgap frequencies to higher values. Due to the similar variations of critical wavenumber versus initial shear modulus contrast, bandgaps for different matrix locking parameters follow the same general trend.0.001.This section further examines the influence of the stiff layer-locking parameter on bandgaps. Figure 5 (a) exhibits the bandgaps in laminates with a Gent stiff layer and a neo-Hookean matrix. Three locking parameters of the rigid layer are 0.1, 0.2, and 1. The volume fraction of the stiff layer is. The bandgaps in Fig. 5 (a) are functions of initial shear modulus contrast. The critical values of instability points for each laminate are included in Fig. 5 (b). The post-buckling deformation level is fixed at.

In contrast to laminates with a Gent matrix and a neo-Hookean stiff layer, those with a Gent stiff layer show highly complex variations in their bandgaps versus the initial shear modulus contrast and locking parameter of the layer. The key distinction lies in the stiffening behavior of the hard Gent layer. When $J_m^{(f)} = 1$, the bandgap disappears at around $k_\mu \approx 50$, similar to all-neo-Hookean ones. The bandgap width decreases with effective shear modulus contrast. However, laminates with $J_m^{(f)} = 0.2$ shows more complicated variations of bandgaps. When $k_\mu \approx 40$, the bandgap first disappears due to the transition of microscopic instability into macroscopic mode. Considering the effective shear modulus contrast is higher at small stiff layer locking parameters given certain deformation levels, it is reasonable to see the disappearance threshold of the bandgap reduce from $k_\mu \approx 50$ with $J_m^{(f)} = 1$ to $k_\mu \approx 40$ with $J_m^{(f)} = 0.2$.

As the initial shear modulus contrast decreases further, the critical stretch reduces and promotes layer stiffening. When the stiffening of the hard layer reaches a certain threshold, the effective shear modulus contrast increases, leading to the reappearance of microscopic instability and also the bandgap between $k_\mu = 5$ and $k_\mu = 8$. At the same time, the highly stiffened

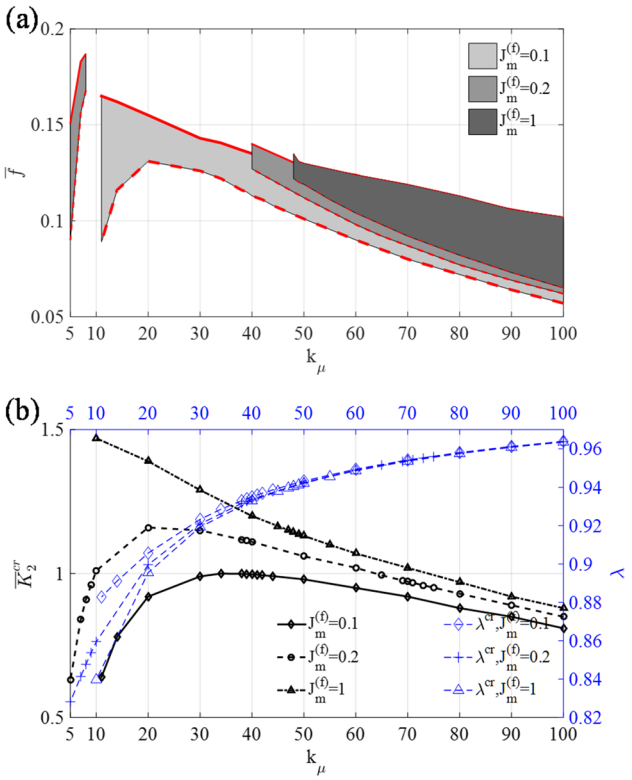

Fig. 5 **a** Bandgaps versus initial shear modulus contrast in the neo-Hookean matrix and Gent stiff layer laminates with $c^{(f)} = 0.06$ and $J_m^{(f)} = 0.1,0.2,1$ at $\Delta\varepsilon = 0.001$; **b** critical stretch and normalized critical wavenumber versus initial shear modulus contrast for laminates in **a**

layer widens the bandgap with increased buckling deformation levels. In the end, the rapid stiffening of the hard layer with $J_m^{(f)} = 0.1$ extends the appearance of the bandgap to $k_\mu \approx 11$, where instability transits into the macroscopic mode. Beyond $k_\mu \approx 30$, the bandgap width decreases with increasing in initial shear modulus contrast. Conversely, for $k_\mu < 30$, a lower initial shear modulus contrast results in a wider bandgap. This phenomenon can also be attributed to the higher buckling deformation level that improves the stiffening of the layer.

4.3 Shear wave bandgaps in all-Gent phase laminates

In this section, we examine the bandgap in all-Gent laminates, where the locking parameters of both phases are identical ($J_m^{(f)} = J_m^{(m)} = J_m$). Figure 6 (a) exhibits the bandgap as a function of the locking parameter J_m, with initial shear modulus contrast of laminate set at $k_\mu = 100$ and the volume fraction of the stiff layer fixed at $c^{(f)} = 0.06$. The corresponding critical instability parameters are shown in Fig. 6 (b).

In this case, the bandgap persists until the instability transforms into macroscopic mode at approximately $J_m \approx 0.047$. For $J_m < 1$, the phases stiffen, enhancing the laminate's stability and leading to buckling at lower critical stretch ratios. The quick stiffening improves the stress and energy levels in the post-buckling state, resulting in an enlargement of the bandgap for $J_m < 1$. The bandgap moves towards lower frequencies, consistent with the tendencies observed in previous sections. Moreover, for $J_m > 1$, the critical stretch ratio and wavenumber curves remain flat. The width of the bandgap varies slightly and its tendency is generally horizontal.

5 Conclusions

In summary, this paper investigates the emergence and influential factors of the post-buckling bandgap for S-waves in soft laminates. The direction of wave propagation is parallel to the stiff layer orientation. In this non-periodic direction, elastic instability acts as a switch that transforms the infinitely extended stiff layer into a periodic wavy form, thereby inducing a bandgap in the post-buckling regime. The bandgap can be activated and deactivated due to the recoverability of soft material based on demand. The only stimulus is the mechanical compression along the layer orientation.

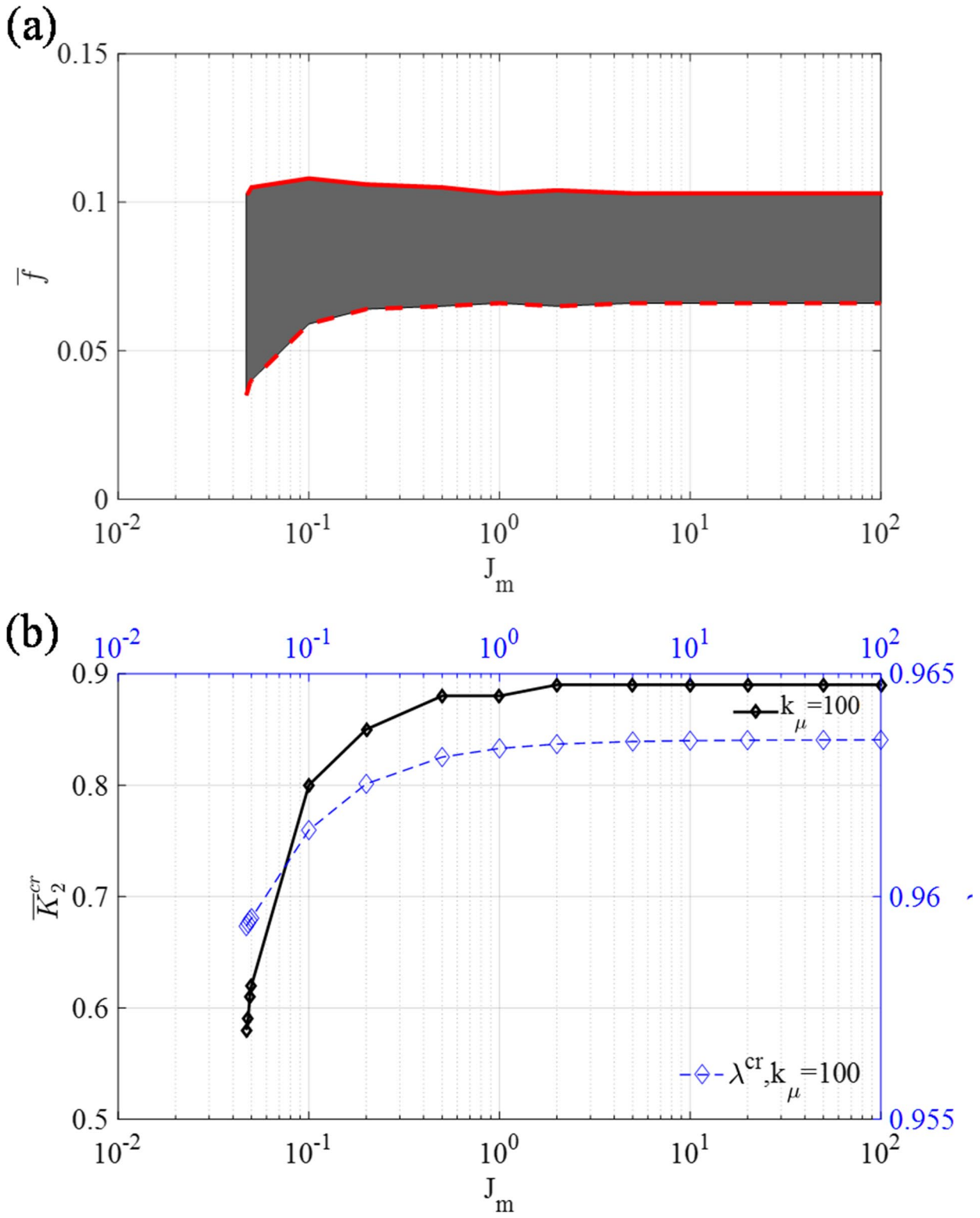

Fig. 6 A Bandgaps versus locking parameter in all-Gent laminates with $c^{(f)} = 0.06$ and $k_{\mu} = 100$ at $\Delta\varepsilon = 0.001$; **b** critical stretch and normalized critical wavenumber versus initial shear modulus contrast for laminates in **a**

We further studied the tuning of post-buckling bandgap by considering the stiffening behavior of phases. The findings highlight that the effective shear modulus contrast is a dominant factor: its decrease narrows the bandgap; its increase shifts the bandgap to lower frequencies by increasing the wavelength. The inclusion of Gent phases that stiffen during deformation induces diverse changes in shear modulus contrast and significantly extends the design domain.

The buckling-activated, recoverable bandgap can be further explored for developing innovative acoustic metamaterial. The structural transition that can induce periodic configurations and activate bandgaps is also available in other infinitely extensible composites [35, 37]. Furthermore, as composite geometries become more complex, the impact of post-buckling behavior on elastic wave modes emerges as a promising area of exploration with significant breadth and depth [41]. We note that studying the influence of imperfections on structural transformation can be an interesting area. We also note that we showed the relationship between bandgap width and effective shear modulus ratio in the pre-buckling states. However, the geometry of buckled laminate leads to nonhomogeneous stress fields, and the influence of stress level is complex. We can extend our study to the relation between post-buckling bandgaps and stress fields.

Appendix A. Decoupling of waves

Due to the coupling of S-wave and P-wave, the following wave ratio is defined to distinguish wave modes.

$$\xi\left(n, \overline{K}_2\right) = \int_{\backslash \mathrm{var}\,\mathrm{vec}\Omega} \frac{|u_1|}{|u_1| + |u_2|} \tag{16}$$

where $u_1 = u_1(\boldsymbol{x})$ and $u_2 = u_2(\boldsymbol{x})$ are the components of displacement in the eigenmode of n-th order eigenvalue and wavenumber $\overline{K}_2$. After the Bloch-Floquet analysis, the wave ratio is calculated for every eigenvalue on the curve $\overline{f}\left(\overline{K}_2\right)$. Setting up a threshold for the wave ratio, the P-wave can be removed from the dispersion curves. This decoupling process is applied in the following sections such that we can focus on the eigenfrequencies and eigenmodes of S-waves.

Author contributions Qi Yao: Writing – review & editing, Writing – original draft, Visualization, Validation, Investigation, Formal analysis, Data curation, Conceptualization. Stephan Rudykh: Writing – review & editing, Writing – original draft, Supervision, Resources, Investigation, Funding acquisition, Conceptualization.

Funding No funding was received for this work.

Data availability The data supporting the findings of this study are openly available and can be provided upon request.

Declarations

Ethics approval and consent to participate Qi Yao and Stephan Rudykh confirm their participation in this research. Ethical approval was not required for this study.

Consent for publication Both authors consent to the publication of this work.

Competing interests The authors declare that they have no competing interests.

References

1. Clausen, A., Wang, F., Jensen, J.S., Sigmund, O., Lewis, J.A.: Topology optimized architectures with programmable Poisson's ratio over large deformations. Adv. Mater. **27**, 5523–5527 (2015)
2. Xin, X., Liu, L., Liu, Y., Leng, J.: 4D printing auxetic metamaterials with tunable, programmable, and reconfigurable mechanical properties. Adv. Funct. Mater. (2020). https://doi.org/10.1002/adfm.202004226
3. Xin, X., Liu, L., Liu, Y., Leng, J.: 4D pixel mechanical metamaterials with programmable and reconfigurable properties. Adv. Funct. Mater. (2022). https://doi.org/10.1002/adfm.202107795
4. Galea, R., Dudek, K.K., Farrugia, P.S., Zammit Mangion, L., Grima, J.N., Gatt, R.: Reconfigurable magneto-mechanical metamaterials guided by magnetic fields. Compos. Struct. (2022). https://doi.org/10.1016/j.compstruct.2021.114921

5. Ke, X., Jang, J., Chai, Z., Yong, H., Zhu, J., Chen, H., Guo, C.F., Ding, H., Wu, Z.: Stiffness preprogrammable soft bending pneumatic actuators for high-efficient, conformal operation. Soft Robot. (2021). https://doi.org/10.1089/soro.2020.0207
6. Melancon, D., Gorissen, B., García-Mora, C.J., Hoberman, C., Bertoldi, K.: Multistable inflatable origami structures at the metre scale. Nature **592**, 545–550 (2021)
7. Guo, X., Ni, X., Li, J., et al.: Designing mechanical metamaterials with kirigami-inspired, hierarchical constructions for giant positive and negative thermal expansion. Adv. Mater. (2021). https://doi.org/10.1002/adma.202004919
8. Brunet, T., Leng, J., Mondain-Monval, O.: Soft acoustic metamaterials. Science **342**, 323–324 (2013)
9. Kruss, N., Paulose, J.: Nondispersive one-way signal amplification in sonic metamaterials. Physical Review Applied **17**, 024020 (2022)
10. Elmadih, W., Chronopoulos, D., Zhu, J.: Metamaterials for simultaneous acoustic and elastic bandgaps. Sci. Rep. (2021). https://doi.org/10.1038/s41598-021-94053-3
11. Cheng, Y., Yang, F., Xu, J.Y., Liu, X.J.: A multilayer structured acoustic cloak with homogeneous isotropic materials. Appl. Phys. Lett. (2008). https://doi.org/10.1063/1.2903500
12. Kaina, N., Lemoult, F., Fink, M., Lerosey, G.: Negative refractive index and acoustic superlens from multiple scattering in single negative metamaterials. Nature **525**, 77–81 (2015)
13. Padilla, W.J., Basov, D.N., Smith, D.R.: Negative refractive index metamaterials. Mater. Today **9**, 28–35 (2006)
14. Lee, S.H., Park, C.M., Seo, Y.M., Wang, Z.G., Kim, C.K.: Acoustic metamaterial with negative density. Physics Letters A **373**, 4464–4469 (2009)
15. Bertoldi, K., Vitelli, V., Christensen, J., Van Hecke, M.: Flexible mechanical metamaterials. Nat. Rev. Mater. (2017). https://doi.org/10.1038/natrevmats.2017.66
16. Shan, S., Kang, S.H., Raney, J.R., Wang, P., Fang, L., Candido, F., Lewis, J.A., Bertoldi, K.: Multistable architected materials for trapping elastic strain energy. Adv. Mater. **27**, 4296–4301 (2015)
17. Kochmann, D.M., Bertoldi, K.: Exploiting microstructural instabilities in solids and structures: from metamaterials to structural transitions. Applied Mechanics Reviews **69**, 050801 (2017)
18. Li, J., Arora, N., Rudykh, S.: Elastic instabilities, microstructure transformations, and pattern formations in soft materials. Curr. Opin. Solid State Mater. Sci. **25**, 100898 (2021)
19. Bertoldi, K., Boyce, M.C.: Wave propagation and instabilities in monolithic and periodically structured elastomeric materials undergoing large deformations. Phys Rev B - Condens Matter Mater Phys (2008). https://doi.org/10.1103/PhysRevB.78.184107
20. Krishnan, D., Johnson, H.T.: Optical properties of two-dimensional polymer photonic crystals after deformation-induced pattern transformations. J. Mech. Phys. Solids **57**, 1500–1513 (2009)
21. Li, J., Pallicity, T.D., Slesarenko, V., Goshkoderia, A., Rudykh, S.: Domain Formations and Pattern Transitions via Instabilities in Soft Heterogeneous Materials. Adv. Mater. **31**, 1807309 (2019)
22. Chen, D., Xiang, Y., Arora, N., Yao, Q., Li, J., Rudykh, S.: Post-buckling development in soft particulate composites. Compos. Struct. **322**, 117337 (2023)
23. Chen, D., Arora, N., Xiang, Y., Li, J., Slesarenko, V., Rudykh, S.: Instability-induced patterns and their post-buckling development in soft particulate composites. Mech. Mater. (2022). https://doi.org/10.1016/j.mechmat.2022.104482
24. Xiang, Y., Chen, D., Arora, N., Yao, Q., Rudykh, S.: Towards understanding the role of viscoelasticity in microstructural buckling in soft particulate composites. Compos. Part B Eng. **263**, 110850 (2023)
25. Combescure, C., Henry, P., Elliott, R.S.: Post-bifurcation and stability of a finitely strained hexagonal honeycomb subjected to equi-biaxial in-plane loading. Int. J. Solids Struct. **88–89**, 296–318 (2016)
26. Mousanezhad, D., Babaee, S., Ebrahimi, H., Ghosh, R., Hamouda, A.S., Bertoldi, K., Vaziri, A.: Hierarchical honeycomb auxetic metamaterials. Sci. Rep. **5**, 18306 (2015)
27. Guttag, M., Boyce, M.C.: Locally and dynamically controllable surface topography through the use of particle-enhanced soft composites. Adv. Funct. Mater. **25**, 3641–3647 (2015)
28. Spinelli, S.A., Lopez-Pamies, O.: Some simple explicit results for the elastic dielectric properties and stability of layered composites. Int. J. Eng. Sci. **88**, 15–28 (2015)
29. Zhu, J., Chen, H., Wu, B., Chen, W., Balogun, O.: Tunable band gaps and transmission behavior of SH waves with oblique incident angle in periodic dielectric elastomer laminates. Int. J. Mech. Sci. **146–147**, 81–90 (2018)
30. Bahreman, M., Arora, N., Darijani, H., Rudykh, S.: Structural and material electro-mechanical instabilities in microstructured dielectric elastomer plates. Eur. J. Mech. **94**, 104534 (2022)
31. O'Neill, M.R., Sessions, D., Arora, N., Chen, V.W., Juhl, A., Huff, G.H., Rudykh, S., Shepherd, R.F., Buskohl, P.R.: Dielectric elastomer architectures with strain-tunable permittivity. Adv Mater Technol (2022). https://doi.org/10.1002/admt.202200296
32. Li, J., Slesarenko, V., Galich, P.I., Rudykh, S.: Oblique shear wave propagation in finitely deformed layered composites. Mech. Res. Commun. **87**, 21–28 (2018)
33. Li, J., Slesarenko, V., Rudykh, S.: Microscopic instabilities and elastic wave propagation in finitely deformed laminates with compressible hyperelastic phases. Eur J Mech A/Solids **73**, 126–136 (2019)
34. Yue, Q., Sangwoo, K., Pence, T.J.: Plane strain buckling and wrinkling of neo-hookean laminates. Int. J. Solids Struct. **31**, 1149–1178 (1994)
35. Galich, P.I., Slesarenko, V., Li, J., Rudykh, S.: Elastic instabilities and shear waves in hyperelastic composites with various periodic fiber arrangements. Int. J. Eng. Sci. **130**, 51–61 (2018)
36. Merodio, J., Ogden, R.W.: Remarks on instabilities and ellipticity for a fiber-reinforced compressible nonlinearly elastic solid under plane deformation. Q. Appl. Math. **63**, 325–333 (2005)
37. Li, G.Y., Zheng, Y., Cao, Y., Feng, X.Q., Zhang, W.: Controlling elastic wave propagation in a soft bilayer system: via wrinkling-induced stress patterns. Soft Matter **12**, 4204–4213 (2016)
38. Liu, J., Bertoldi, K.: Bloch wave approach for the analysis of sequential bifurcations in bilayer structures. Proceedings of the Royal Society A: Mathematical, Physical and Engineering Sciences (2015). https://doi.org/10.1098/rspa.2015.0493

39. Ogden, R.W.: Non-linear elastic deformations. Dover Publications, New York (1997)
40. Yao, Q., Arora, N., Chen, D., Xiang, Y., Rudykh, S.: Elastic instabilities of soft laminates with stiffening behavior. Appl. Math. Model. **130**, 658–675 (2024)
41. Galich, P.I., Sharipova, A., Slesarenko, S.: The emergence of sequential buckling in reconfigurable hexagonal networks embedded into soft matrix. Materials (Basel) **14**, 1–13 (2021)